Nano Energy 42 (2017) 129–137

Contents lists available at ScienceDirect

Nano Energy

journal homepage: www.elsevier.com/locate/nanoen

Full paper

Digitalized self-powered strain gauge for static and dynamic measurement

Zongming Su[a], Hanxiang Wu[a], Haotian Chen[b], Hang Guo[b], Xiaoliang Cheng[a], Yu Song[a], Xuexian Chen[b], Haixia Zhang[a,b,*]

[a] National Key Laboratory of Science and Technology on Micro/Nano Fabrication, Institute of Microelectronics, Peking University, Beijing 100871, China
[b] Academy for Advanced Interdisciplinary Studies, Peking University, Beijing 100874, China

ARTICLE INFO

Keywords:
Self-powered sensor
Triboelectric nanogenerator
Strain gauge
Motion sensor
Human motion detection

ABSTRACT

This paper presents a digitalized self-powered triboelectric strain gauge (DSSG) for the first time. Different from conventional resistive or capacitive analogue strain responsive mechanisms, adopting the output of grated triboelectrication as sensing signal for static and dynamic strain measurement allows for digitalized strain measurement with excellent accuracy, sensitivity and linearity. Instead of analyzing voltage/current value of sliding-mode triboelectric nanogenerator (S-TENG) to evaluate strain, the DSSG exploits a grated triboelectric electrode to generate periodical output signals when the designed elastomer has relative movement with the grated electrode. A promoted real-time analysis system (RAS) enables the analysis and display of the digitalized signals. Benefiting from the micro-manufacturing techniques of grated electrode, DSSG reaches a remarkable gauge factor as high as 130 with optimized design of geometrical parameters. The results of static strain measurement prove the feasibility of using such DSSG as a self-powered transducer of tensile forces, with a minimum resolution for tensile force detection of 120 mN per cycle. At the same time, dynamic strain sensing assisted by signal processing system provides possibility of using such DSSG for real-time elbow joint motion detection and posture analysis, thereby indicating its great potentials for human-machine interface, prosthetic, and biomechanical applications.

1. Introduction

Stretchable and wearable electronics have attracted tremendous attention recently due to their abilities for monitoring and interacting with human body [1] and soft robotic [2]. Material, structural and fabrication advancements have uncovered a diverse set of flexible and stretchable devices with different functions [3,4], where strain sensing is one of the key technique. Strain sensor is the device that transduces mechanical deformations into electrical signals, which can typically be classified into two main strategies: resistive-type and capacitive-type.

Resistive-type sensors are mainly composed of sensing film with resistive sensitivity coupled onto stretchable substrates [5–10]. The electrical conductive film has resistive change as a function of applied strain when the composite film is stretched by external force. Based on different mechanisms, such as piezoresistive [5], disconnection mechanism [9], and crack propagation [7], the gauge factor (*GF*) can change in a wide range (from less than 1 [10] to 2000 [6]). Generally, stretchable strain sensors based on microcrack and disconnection mechanisms have higher sensitivity than other mechanisms. Although there are many strategies to choose from for high *GF*, nonlinear resistive response is one of the main drawbacks of most resistive-type devices, which is also the reason that makes calibration process difficult and complex [6,8]. By contrast, capacitive-type sensors usually incorporate a sandwiched structure (a conductive layer, a dielectric layer and another conductive layer) [11–13]. When the sensors are applied with strain, the thickness reduction of dielectric layer results in the increase of the capacitance [12]. With this geometrical-effect-based mechanism and the linear mechanical deformation of stretched material, capacitive-type sensor typically has linear responsive output [11,13]. However, they usually have very low sensitivity ($GF \leq 1$) due to theoretical limitations. Overall, a trade-off relationship between high sensitivity and high linearity needs to be considered for most of the resistive and capacitive strain sensing systems. In addition to these two passive strain sensing mechanisms, piezoelectric strain sensors [14,15], which rely on piezoelectric materials and enable mechanical-to-electrical energy conversion, also attracts attention in recent years. Although with ultrafast response, high sensitivity, and low power consumption, relatively low flexibility and stretchability restricts piezoelectric strain sensors in practical applications, especially on wearable electronics.

Recently, triboelectric nanogenerator (TENG) has shown great potential in mechanical energy harvesting [16,17] as well as sensing of external stimulus including pressure [18], vibration [19], movements

* Corresponding author at: National Key Laboratory of Science and Technology on Micro/Nano Fabrication, Institute of Microelectronics, Peking University, Beijing 100871, China.
E-mail address: zhang-alice@pku.edu.cn (H. Zhang).

http://dx.doi.org/10.1016/j.nanoen.2017.10.004
Received 25 August 2017; Received in revised form 27 September 2017; Accepted 2 October 2017
Available online 24 October 2017

[20], *etc*. Electrical voltage (or other direct output) has been widely used as a responsive signal to reflect the external stimulus [18–21]. However, TENG is sensitive to quite a lot other parameters such as The uncontrollable external environment [22], random charge distribution [23] and incidental electrostatic discharge [24], thus making the output instability a remarkably tough issue that greatly challenge teh sensing accuracy, stability and durability of the sensing device. A recent work that puts the TENG into vacuum can avoid the humidity change, dust adhesion, and air breakthrough, *etc* [25]. However, this specific environment requirement greatly limits practical applications. Instead of detecting direct output voltage of TENG, an alternative choice is to analyze operation cycles of TENG in a well-designed system [26], because the number of output cycles is insensitive to unexpected external stimulus, e.g., humidity. Calculating the output cycles rather than the exact value of output inspires various self-powered sensors including one dimensional motion sensor [27] that measures position and velocity, rotating angle sensor [28] that detects angular velocity/acceleration.

Herein, we propose a self-powered and digitalized strain gauge that can minimize the influence of environmental fluctuations by analyzing periodic signals of a well-designed S-TENG. Such device consisting of a flexible grated electrode and a stretchable elastomer with two specially designed protrusions. Digitalizing the obtained periodic triboelectric signals enables strain measurement with high sensitivity and accuracy in both static and dynamic modes. Compared with resistive- or capacitive- type strain sensor, a different triboelectric-based mechanism results in high-resolution strain sensing with a minimum resolution of 0.77%. Besides, we have presented a real-time analysis and displaying system for dynamic signal detection, data processing and result presenting, with capabilities in real-time human joint motion detection, posture analysis and real-time demonstration.

2. Experimental

2.1. Design and fabrication

Fig. 1a illustrates the structure diagram of DSSG, which consists of stretchable part with protrusions and flexible part with grated electrode (geometrical parameters of the device are marked in the figure). The stretchable part is made of commonly used elastomer (polydimethylsiloxane, PDMS) and have two protrusions on each side of the membrane. The distance between two protrusions (L) have been set as 42 mm and 65 mm in the experiments. The radius of two protrusions is set as r = 2 mm, while the width (W) and thickness of the elastomer are 20 mm and 2 mm, respectively. In the fabrication process, PDMS base and cross-linker (Sylgard 184, Tow Corning) are thoroughly mixed in a 10:1 ratio (w/w). Proper amount of liquid mixture is then added into one of the concave part of alumimum mold prepared by 3D-printing technology (Fig. S1a(i) in Supporting Information). After solidification of PDMS, the conductive composite is fabricated on its surface to form the conductive elastomer. Afterwards, another liquid PDMS mixture is poured into the as-fabricated conductive compostie as well as residual

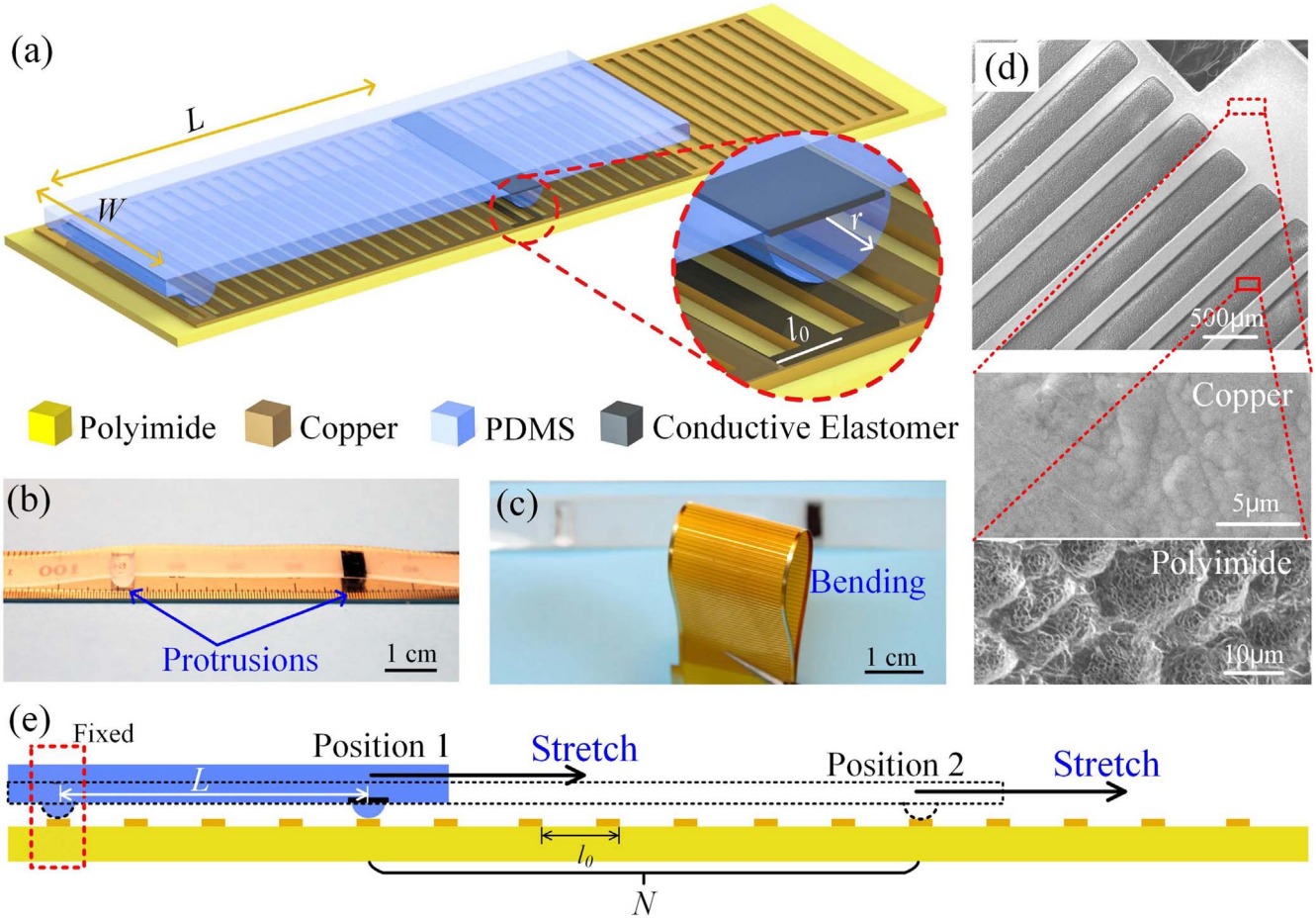

Fig. 1. Structure of the digitalized self-powered strain gauge (DSSG). (a) Schematic view of the pairs of DSSG and detailed information of layers illustrated in the inset. (b, c) Optical photograph of as-fabricated stretchable elastomer with two half-cylinder protrusions (r = 2 mm, W = 20 mm) and flexible grated electrode (l_o = 1 mm). The protrusions can hold the membrane freestanding. (d) ESEM images of grated electrode (top right corner is the pad for electrode extraction) and the enlarged surface morphology of copper and polyimide. (e) A diagram of the operating scheme of DSSG. The left protrusion is clamped onto the surface of the grated electrode, while the right one can be stretched. L is the original distance between two protrusions. N is the cycles that the right protrusion slides across the grated electrode.

surface of aluminum mold and is kept in low-pressure container (< 10 Pa) for 10 min. This low-pressure environment provides a pressure gradient for the air trapped in conductive composite to extract air completely. The liquid PDMS mixture is then solidified at 90 ℃ for 1 h, after which the composite is gently peeled off from the substrate.

It is worth noticing that sandwiching the conductive elastomer, which is made of immobilized multiwall carbon nanotube (MWNT) by polystyrene sphere (PSs) array and PDMS (MWNT/PSs/PDMS), by two PDMS layers improves stretchability, promotes the quality of encapsulation, and facilitates electrostatic induction for signals of STENG. Here, PS spheres can assist the assembly of MWNT networks. The fabrication process of MWNT/PSs networks follows two steps. First, the 3 μm PS spheres with a concentration of 10 wt% are suspended in DI water, in the meanwhile, MWNTs and the same amount of sodium dodecyl benzene sulfonate (SDBS) are added into DI water (1 mg/mL). Two suspensions are mixed by ultrasound for three hours, after which the two suspensions are mixed at the ratio of 1:5 (v:v) and treated by ultrasound for one hour. Second, the mixed suspension is dipped onto glass substrate. The solvent evaporates at 70 ℃ and leaves MWNTs/PSs onto the substrate forming the conductive pathway. The thickness of MWNTs/PSs can be adjusted by the amount of MWNTs/ PS suspension, which is fixed at 100 μL per square centimeter in our experiment.

The grated electrode part is a flexible printed circuit board (FPCB) with grated copper electrode on one side. The period of each grating (l_0) has two values: 0.5 mm and 1 mm. The gap between each grating is 0.3 mm and 0.6 mm, respectively. The size of the grated electrode is 40 mm × 120 mm. Standard FPCB process creates flexible grated electorde. In detail, a 50-μm-thick polyimide (PI) substrate is prepared to attach to copper thin film (50 μm) by epoxy adhesive. The copper films is then patterned by photolithography and etched by $FeCl_3$ solution. The samples are rinsed in DI water for 3 times and dried in nutrigen for use.

2.2. Characterization and mechanism

Fig. 1b and c show the two as-fabricated parts, respectively. Designing the size of the protrusions as well as the distance between them is essential to support the membrane as shown in Fig. 1b. The membrane has no contact with the grated electrode below at both original and stretched states. The grated electrode shown in Fig. 1c is fabricated on flexible substrate so that it can be bend and attached onto curved surfaces, such as human skins. The grated electrode, as well as its enlarged images of copper and polyimide surfaces are characterized using environment scanning electron microscope (ESEM, FEI Quanta 600) as shown in Fig. 1d. The period of the gratings is kept the same for one sample. During practical operation of the device, the protrusion without conductive elastomer is clamped onto the surface of grated electrode as illustrated in Fig. 1e. The right end of the elastomer can be stretched and the right protrusion slides across surface of the substrate and passes N cycles of grates from Position 1–2.

Considering the simplified circumstance when the protrusion slides across one grating cycle as shown in Fig. 2a and b, the protrusion begins at the fully contact position (i). Two opposite and balanced charges generate on both surface because of triboelectrification (negative charges on PDMS surface while positive charges on the grated electrode [29,30]). Fig. 2b(i) shows its electrostatic voltage distribution over the model by finite element simulation method. When the protrusion continuously moves to the right, the equilibrium is broken. As a result, the immobilized charges on PDMS surface leads to charge rebalance through charge transfer on external circuit (Fig. 2a(ii)). The direction of charge transfer is reversed at the middle of the gap where the open-circuit voltage reach its peak value due to the maximum deviation of both electrode lattices (Fig. 2a(iii) and b(iii)). Fig. 2c shows the simulated open-circuit voltage versus protrusion position, with marked position i, ii and iii, in comparison with the experimental results under 100 MΩ load in Fig. 2d. The great electrical value difference is because the simulated result is obtained at open circuit condition and the experimental case is tested under limited load. Besides, insufficient contact in experimental condition contributes less surface charge on contact surfaces.

Further investigation focuses on the mechanical characteristic of the elastomer membrane with two designed protrusions. From the stress distribution in Fig. 2e, two protrusions have little effect on that of the flat membrane. For close investigation of the stress distribution, two selected points (A and B) at key positions have been picked up and their strain and stress are illustrated in Fig. 2f, which show that Point A has corresponding strain change with elongation, while Point B has a slight increase (stress) or decrease (strain) because of surrounding stress. The results verify that the protrusions have limited influence on strain and stress of the flat membrane. At the same time, conductive elastomer in the protrusion can work effectively because of little stress interruption.

2.3. Mechanical and electrical test

Before mechanical and electrical test of DSSG, the flexible grated electrode was attached onto a polymethyl methacrylate (PMMA) block by double-side tape. At the same time, one protrusion of the elastomer is clamped onto the grated electrode. A tension tester (HSV, HANDPI) was used to stretch the elastomer at a certain velocity, meanwhile a pull and push dynamometer (HP-50, HANDPI) is applied to measure the tensile force during elongation. In particular, the stretch direction has been set to be parallel to the plane of grated electrode in order to ensure the necessary contact between protrusion and grated electrode. The contact force is applied by its own weight of the elastomer for smooth sliding. The output voltage was amplified by low-noise voltage preamplifier (SR560, SRS) and then measured by a digital oscilloscope (DS1102E, RIGOL) at 100 MΩ external load. All simulated and experimental data of the electrical performance are treated to alternating voltage/current for better comparison, as the direct parts of the signals are not stable enough for each test and cause difficulties to data analysis. Besides, environmental noise of all experimental data is removed by a digital filter.

3. Results and discussions

3.1. Electrical measurement

Samples with different parameters (different L and l_0) serve as devices for thorough investigation of the performance. The output voltages of STENG in Fig. 3a and b show periodic quasi sine waveforms with 26 cycles and 11 cycles, respectively, indicating that the device can generate electrical outputs under different elongations. Besides the voltage waveforms, which are mainly investigated in most experiments, short-circuit current shown in Fig. 3c can also provide similar information. When we compare the waveforms in Fig. 3a, b and c, the maximum values of each figure is different but has no influence on the results because only the numbers of cycles are calculated. The number of output cycles (voltage or current) of STENG, which is insensitive to exact output of STENG in different environments, can be digitized from analogue waveform and thus greatly improve its strain sensing accuracy. Considering the geometrical relationship that sliding distance of the protrusion is equal to the elongation of the elastomer, strain of the device can be achieved by the number of output cycles (N) (Fig. 3d), which have a linear relationship between strain of membrane and N. In other words, the strain of the membrane can be directly obtained if output cycles is known. Fig. 3e illustrates the position and voltage waveform during the whole process when the device was stretched and then released it to original state.

3.2. Gauge factor

Based on the result that the sensing function is consistent with the geometrical parameters, DSSG with higher sensitive is also possible with optimization by selection of these parameters. Gauge factors are given by

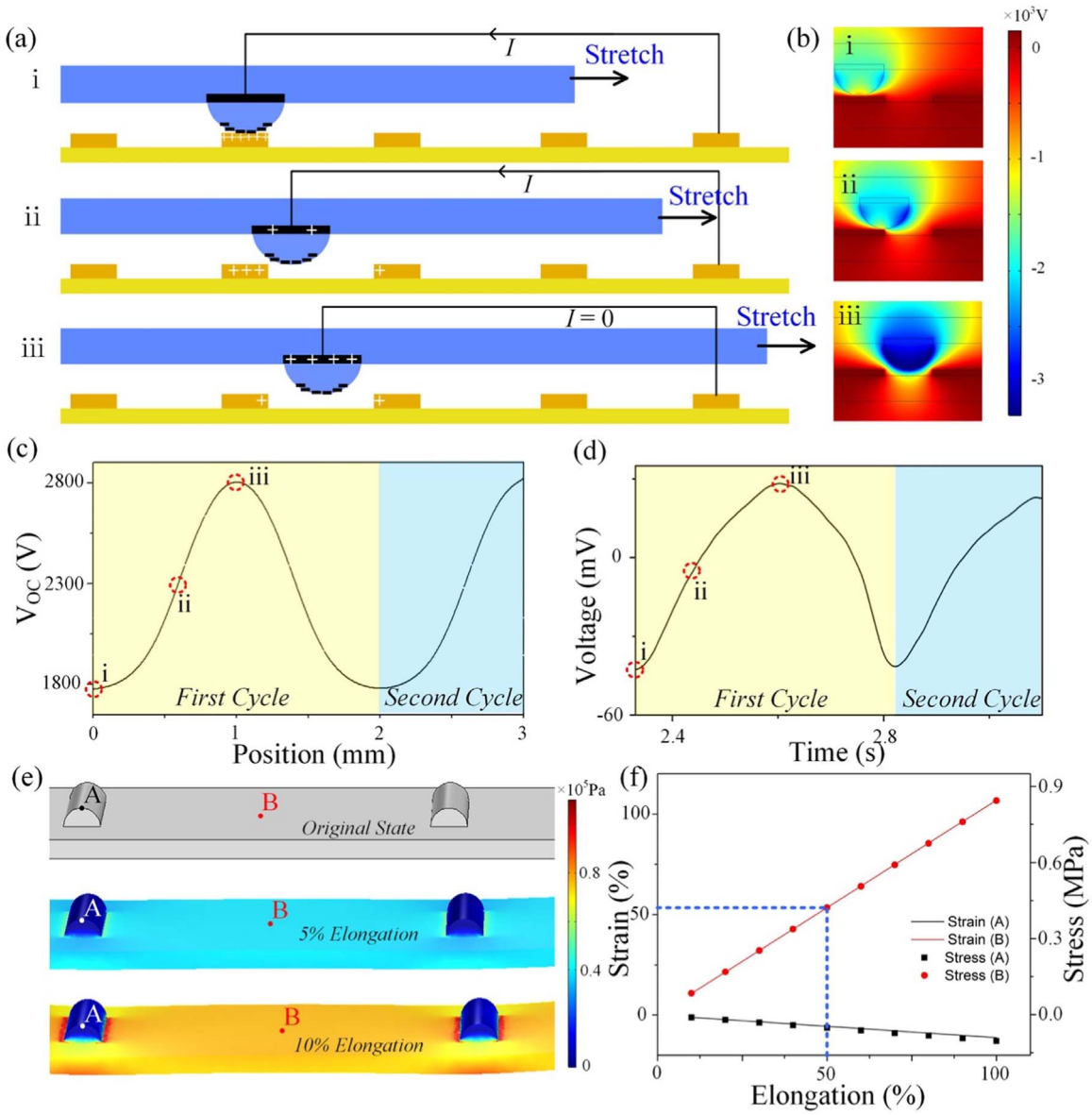

Fig. 2. Working principle of DSSG. (a) Sketches illustrate relatively moving between the protrusion and the grated electrode. The opposite charges are generated because of triboelectrification and flow in the external circuit when the relative movement happens due to electrostatic induction (Position i, ii and iii). (b) Distribution of open-circuit electric potential when the protrusion slides from Position i to iii. (c, d) Simulated open circuit voltage and experimental voltage result of S-TENG during the movement of first cycle and the second cycle, respectively. Position i, ii and iii has been marked in both graphs. (e) Simulation of stress distribution when the elastomer with protrusions is stretched (5% and 10%). The flat membrane part (*e.g.,* Point A) shares most stress equally while there is barely stress (*e.g.,* Point B) on top of two protrusions. (f) Strain and stress versus elongation on two specific points (A and B) illustrated on (e): Point A has corresponding strain change with the elongation, while Point B has a slight decrease because of surrounding stress.

$GF = (\Delta R/R_0)/\varepsilon$ and $GF = (\Delta C/C_0)/\varepsilon$ for resistive-type and capacitive-type sensors, respectively, where ΔR (or ΔC) is the resistance (or capacitance) change, R_0 (or C_0) is the original resistance (or capacitance), ε is the strain during elongation. In the equations, $\Delta R/R_0$ and $\Delta C/C_0$ are both relative change that can reflect the sensitivity of the device. For DSSG, the digitalized output cycles (N) plays the same role. Thus, we define the gauge factor of DSSG as:

$$GF = \frac{N}{\varepsilon} \tag{1}$$

Considering the geometrical relationship:

$$L \bullet \varepsilon = N \bullet l_0 \tag{2}$$

$$GF = \frac{N}{\varepsilon} = \frac{L}{l_0} \tag{3}$$

At the same time, resolution (α) of the device reflect the minimum strain change that one cycle can sense. It is given as:

$$\alpha = \frac{\varepsilon}{N} = \frac{l_0}{L} = \frac{1}{GF} \tag{4}$$

In Eqs. (3) and (4), only two geometrical parameters decide *GF* and resolution of DSSG (L and l_0). Specifically, a smaller l_0 and a larger L give a higher *GF*. In simulation, l_0 has been altered from 2 to 1 mm, resulting in the increase of electrical cycles so as to enhance *GF* of DSSG (See Supplementary Discussion). In the experiments, we fabricated several samples with different parameters (l_0 and L). The theoretical relationships between strain and N with different geometrical designs are illustrated in Fig. 3f, together with the well consistent experimental results. For L = 65 mm, l_0 = 0.5 mm, the resolution is 0.77% per cycle and GF = 130, while for L = 42 mm, l_0 = 1 mm, the resolution is 2.38% per cycle and *GF* is only 42.

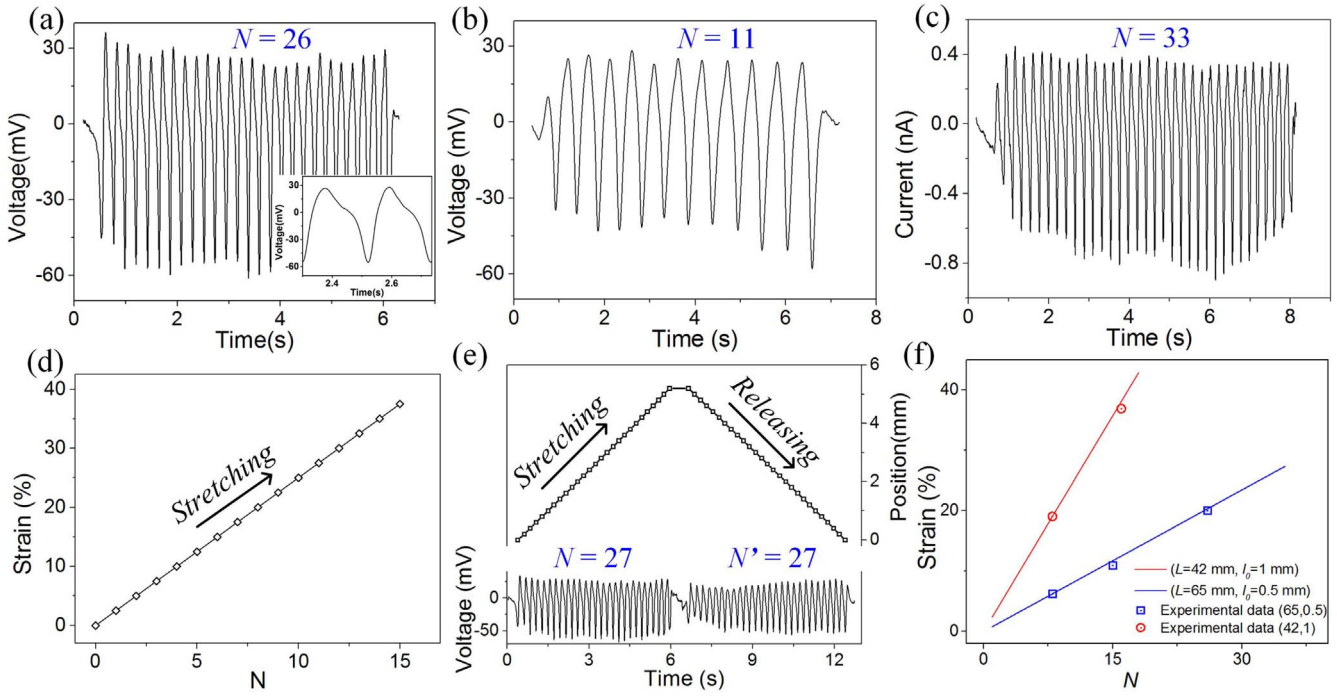

Fig. 3. Digitalized output characteristic of DSSG by calculating output cycles. (a, b) Voltage of STENG with 26 cycles and 11 cycles that illustrate large and small strain during different elongation processes, respectively (under 100 MΩ load). (c) Short circuit current of STENG with 33 cycles, indicating that both voltage and current outputs can be utilized for digitalized analysis. (d) Linear strain response versus digitalized output cycles during elongation. (e) The positions of protrusion and output voltage during both stretching and releasing processes. (f) Parameter analysis of different L and l_0 for high sensitive strain detection. The dots represent the experimental results which is corresponding well to theoretical results represented by solid lines.

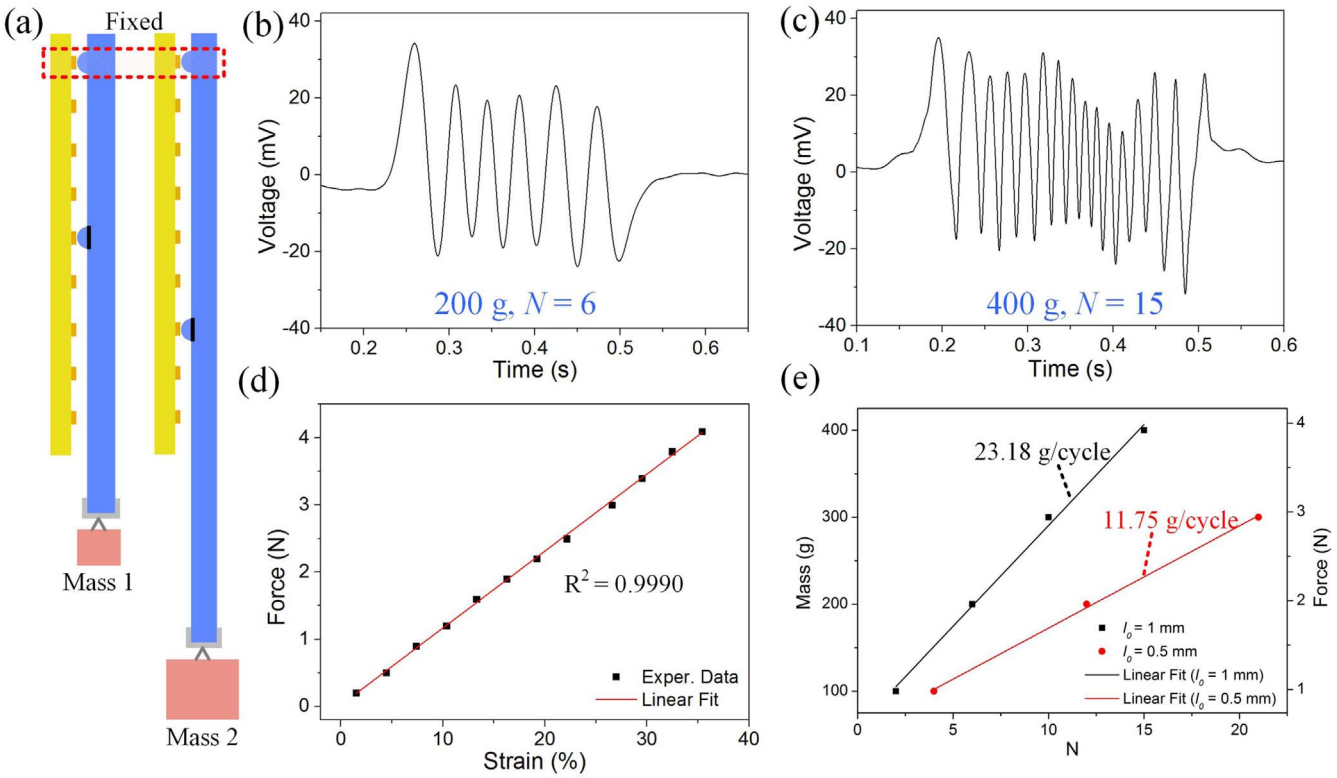

Fig. 4. The DSSG serves as force measurement and functions as a digital dynamometer. (a) The schematic diagram of dynamometer with different weighing objects. (b, c) The electrical output waveforms when measuring 200 g and 400 g objects. (d) The applied force with increased strain and the linear fit of the experimental results. (e) The demonstration of digital dynamometer with experimental result and its linear fit with different geometrical parameters (l_0 at 0.5 mm and 1 mm have different resolutions of 23.18 g/cycle and 11.75 g/cycle, respectively).

According to its definition, *GF* of DSSG can increase without limitation by extreme geometrical design. However, with the increase of L, the space occupation of the sensor increases linearly. To overcome this problem, a modified definition of gauge factor (*GF'*) by considering its space consumption, which is commonly used in the digit-display technology,[] is given by:

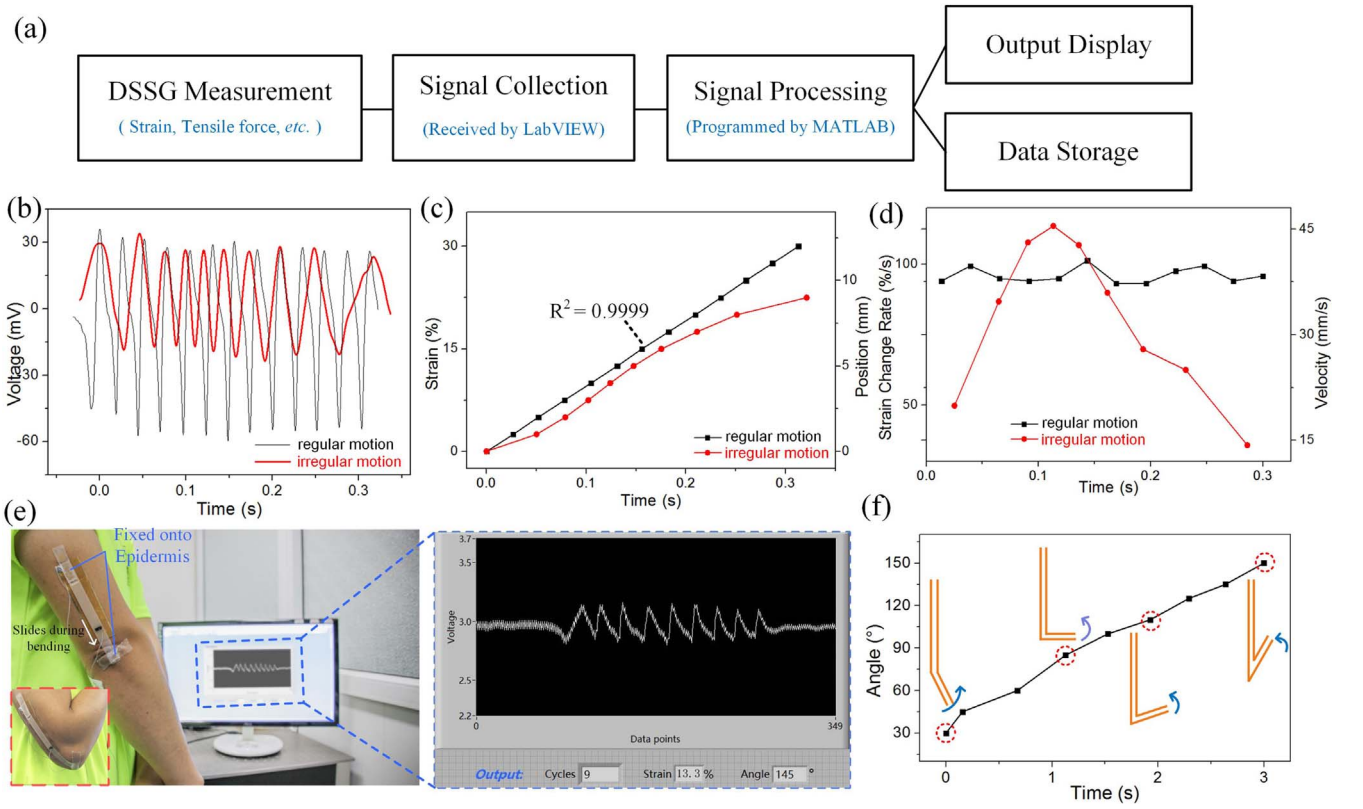

Fig. 5. Dynamic strain measurement of DSSG. (a) Diagram of real-time analysis system consisting of four parts. (b) Two electrical output waveforms of different motions (the black curve is the preset regular motion, and the red curve is the irregular motion). (c) Dynamic strain and displacement change with time. R^2 = 0.9999 for regular motion. (d) Strain changing rate and velocity change with time. The calculated rate and speed tell the exact velocity value of the protrusion. The small velocity fluctuation has been observed for regular motion. (e) DSSG works as the epidermal sensor for real-time detection of joint movement (The inset is the joint after bending). The enlarged display-window showing the electrical output as well as results (electrical cycles, applied strain and bending angle) by real-time analyzing system. (f) Reestablishment of arm bending postures by recorded data from dynamic bending process.

$$GF' = \frac{N}{\varepsilon} \times \frac{1}{L} = \frac{1}{l_0} \tag{5}$$

In Eq. (5), *GF'* is only related to the period of grating. If l_0 is 0.5 mm, *GF'* equals 2mm^{-1}. Although this definition changes the dimension of gauge factor compared to traditional methods which is dimensionless, it gives a much practical concept in digital sensing field. Supplementary illustrations of detailed simulation (*e.g.*, with other parameters) and experimental results (*e.g.,* different testing speeds) are shown in Figs. S3 and S4 in Supporting Information.

3.3. Tensile force measurement

With well-established sensing system by S-TENG, an ultra-small strain detection method by digitalized cycles has been proved above. At the same time, a tensile force measurement system named as a self-powered digital dynamometer (SDD) has been demonstrated for practical application benefiting from the static sensing results of S-TENG device.

As is illustrated with mechanical properties of the membrane in Fig. 2e and f, the flat membrane shares main elongation and the designed elastomer approximately obeys Hooke's Law [31]. According to detailed derivation in Supplementary Discussion, the applied force (*F*) on the elastomer (when the friction is ignored) is given by:

$$F = \frac{SEl_0}{L}N \tag{6}$$

where *S* is the cross sectional area of the elastomer and *E* is its elastic modulus. Thus, it has a linear relationship with *N* within elastic limit of elastomer.

The basic mechanism is shown in Fig. 4a, which indicates that the mass with higher weight can stretch the elastomer to higher elongation and thus produces more output cycles of S-TENG. The measured object provides the tensile force ($F = mg$, where m is the mass of the measured object, g is the gravitational acceleration). Similar to Eq. (5), the measured mass (m) is given by:

$$m = \frac{SEl_0}{gL}N \tag{7}$$

The maximum weight limit and further theoretical analysis of SDD are shown in Supplementary Discussion.

For practical use of SDD, the calibration process by different weights is shown in Fig. 4b and c. Two different outputs of 6 cycles and 15 cycles for 200 g and 400 g objects have been detected, respectively, in which the digital dynamometer has easy readout because of high signal to noise ratio (The noise of voltage is shown in Fig. S6). To avoid errors by multiple bounds of the mass when hung onto the elastomer, an effective method is to measure its weight when it is taken away. The applying force of the stretchable elastomer as a function of strain is illustrated in Fig. 4d, which has a linear relationship in the range of 0–35%. Besides, different geometrical designs of the device and their influence on the resolutions have been studied. The results in Fig. 4e reveal two linear relationships between output cycles (*N*) and mass of weighing objects. With different geometrical designs (l = 0.5 mm for red line and l = 1 mm for black line), the red linear fit line has a higher resolution of 11.75 g cycle^{-1} than the black linear fit line of 23.18 g cycle^{-1}. The linear results have demonstrated the possibility to utilize static strain sensing results for mass measurement in practical applications. The 1000 times repeated test of the elastomer shown in Fig. S5 in Supporting Information has proved its long-term reliability for sensing task without recalibration.

3.4. Posture analysis of joint movement

Posture analysis is of vital importance to smart human-machine interface [32], soft robotics [1] and virtual reality technology [33]. However, overshooting phenomenon [34,35] in both resistive-type and capacitive-type sensors results in inaccuracy when the stress is suddenly reserved due to the viscoelasticity of elastomer. Here, by analyzing the dynamic output of DSSG, we demonstrate the possibilities and advantages of applying triboelectrification as the strain sensing mechanism for posture analysis.

As shown in Fig. 5a, a real-time analyzing system, consisting of four different parts: DSSG measurement, signal collection, signal processing and output display (or storage), has been established by commercial software: LabVIEW (National Instruments, USA) and MATLAB (MathWorks, USA). Assisted by this system, the dynamic strain sensing for two different moving processes of regular motion (uniform velocity) and irregular motion (variable speed) have been tested and analyzed in Fig. 5b, c and d. Specifically, the feature information (peak, valley and cycle) have been obtained and be used for dynamic strain calculation. The instant strain and positional result shown in Fig. 5c confirm the two different preset movements, which show R-square of 0.9999 for linear fitting of regular motion. To evaluate the strain change during elongation process, we define strain change rate (strain change per second) as a criteria. The calculated strain change rate (or movement velocity of protrusion) in Fig. 5d proves small fluctuation of velocity for regular motion and maximum strain change rate (113.63%/s at 0.10 s) for irregular motion.

For real-time posture analysis, the DSSG is mounted onto human arm in Fig. 5e. The flexible grated electrode is attached onto upper arm, while two ends of the stretchable elastomer are fixed on upper arm and elbow joint, respectively. A slight stretch of the elastomer before fixation is required to guarantee good contact of the two surfaces when the arm is fully straightened. Afterwards, when the arm bends, the elastomer is stretched and slides across the grated electrode. The output signals are acquired by RAS and information of output cycles, strain and bending angle of forearm can be directly read on LabVIEW window. The bending angle, which is obtained based on the data of multiple tests and is preset in the system, can be easily acquired in data matching process. The corresponding relationship between bending angle and operation time is shown in Fig. 5f, and dynamic bending process can be recorded and reestablished based on the feature of the electrical curves. With the above data acquired from the strain gauge by RAS, many moving parameters such as bending angle and bending speed can be easily obtained for real-time human joint movement detection and posture analysis. The experimental videos of general test and elbow joint movement test can be obtained in Supporting Videos.

The overshoot behavior, which was reported for both resistive-type and capacitive-type stretchable sensors due to the stress relaxation of polymers, is absent in this detection mechanism. That is because stress relaxation in viscoelastic material has effect on stress distribution, while causing no change in the length of the elastomer. As a consequence, protrusion does not slide during its stress relaxation. In other words, stress or strain has no effect on the basic sensing part in this device: the grated electrode. Furthermore, the unidirectional bending detection in Fig. 5f can be improved to detect both bending and unbending gestures by small change in design of grated electrode illustrated in Fig. S7.

4. Conclusion

Aiming at high sensitive strain sensing, this article presents a self-powered strain gauge with digitalized output characteristic and high linearity. Exploiting triboelectrification as the responsive mechanism, each STENG generates electrical output with continuous cycles that can be digitalized for accurate both static and dynamic strain measurement. Optimizing geometrical parameters and fabrication using advanced micro-manufacturing techniques enables the DSSG to reach a remarkable gauge factor of 130. The self-powered dynamometer, which utilizes the digitalized cycles of DSSG for mass measurement, demonstrates a resolution of 11.75 g per cycle. For real-time display of the sensing results, we developed a digital processing system capable of data generation, data acquisition, data analysis and data display (and storage) for actual and real-time applications for human joint motion detection and posture analysis.

In comparison with the conventional resistive or capacitive strain sensing mechanism, the proposed detection method has several main advantages. First of all, DSSG provides electrical output itself and can work effectively with no necessity of external power supply unlike the conventional ones. In the second place, DSSG has a digitalized output characteristic which not only benefits from data processing, transmission and storage, but also prevents the effects of possible environmental uncertainties. Besides, DSSG has an adjustable, comparatively high gauge factor and a linear response to applied strain, whereas the conventional ones inevitably involve a trade-off relationship between “high sensitivity” and “high linearity”. Moreover, DSSG can effectively get rid of overshoot behavior because its functional element is not the elastomer but the grated electrode that has no viscoelasticity. Compared with piezoelectric strain sensor, DSSG has a much larger sensing range and have the capability to be flexible and stretchable, which makes it suitable for wearable applications. With all these advantages, the proposed method provides a feasibility for strain sensing applications demanding high accuracy, high sensitivity, high linearity and low power consumption.

Acknowledgment

The author would like to thank Dr. Mengdi Han in Northwestern University for polishing English language and proofreading the article. This work is supported by National Key Research and Development Program of China (2016YFA0202701), and the National Natural Science Foundation of China (Grant No. 61674004 and 91323304), and the Beijing Natural Science Foundation of China (Grant No. 4141002).

Appendix A. Supplementary material

Supplementary data associated with this article can be found in the online version at http://dx.doi.org/10.1016/j.nanoen.2017.10.004.

References

[1] M.L. Hammock, A. Chortos, B.C.K. Tee, J.B.H. Tok, Z. Bao, 25th anniversary article: the evolution of electronic skin (e-skin): a brief history, design considerations, and recent progress, Adv. Mater. 25 (2013) 5997–6038.
[2] S. Kim, C. Laschi, B. Trimmer, Soft robotics: a bioinspired evolution in robotics, Trends Biotechnol. 31 (2013) 287–294.
[3] C. Pang, G.-Y. Lee, T.-i. Kim, S.M. Kim, H.N. Kim, S.-H. Ahn, K.-Y. Suh, A flexible and highly sensitive strain-gauge sensor using reversible interlocking of nanofibres, Nat. Mater. 11 (2012) 795.
[4] Y. Sun, H.H. Wang, High-performance, flexible hydrogen sensors that use carbon nanotubes decorated with palladium nanoparticles, Adv. Mater. 19 (2007) 2818–2823.
[5] M. Amjadi, A. Pichitpajongkit, S. Lee, S. Ryu, I. Park, Highly stretchable and sensitive strain sensor based on silver nanowire–elastomer nanocomposite, ACS Nano 8 (2014) 5154–5163.
[6] D. Kang, P.V. Pikhitsa, Y.W. Choi, C. Lee, S.S. Shin, L. Piao, B. Park, K.-Y. Suh, T.-i. Kim, M. Choi, Ultrasensitive mechanical crack-based sensor inspired by the spider sensory system, Nature 516 (2014) 222–226.
[7] M. Li, H. Li, W. Zhong, Q. Zhao, D. Wang, Stretchable conductive polypyrrole/polyurethane (ppy/PU) strain sensor with netlike microcracks for human breath detection, ACS Appl. Mater. Interfaces 6 (2014) 1313–1319.
[8] X. Li, R. Zhang, W. Yu, K. Wang, J. Wei, D. Wu, A. Cao, Z. Li, Y. Cheng, Q. Zheng, Stretchable and highly sensitive graphene-on-polymer strain sensors, Sci. Rep. 2 (2012) 870.
[9] F. Xu, Y. Zhu, Highly conductive and stretchable silver nanowire conductors, Adv. Mater. 24 (2012) 5117–5122.
[10] T. Yamada, Y. Hayamizu, Y. Yamamoto, Y. Yomogida, A. Izadi-Najafabadi, D.N. Futaba, K. Hata, A stretchable carbon nanotube strain sensor for human-motion detection, Nat. Nanotechnol. 6 (2011) 296–301.
[11] L. Cai, L. Song, P. Luan, Q. Zhang, N. Zhang, Q. Gao, D. Zhao, X. Zhang, M. Tu,

F. Yang, Super-stretchable, transparent carbon nanotube-based capacitive strain sensors for human motion detection, Sci. Rep. 3 (2013) 3048.
[12] X. Cheng, B. Meng, X. Chen, M. Han, H. Chen, Z. Su, M. Shi, H. Zhang, Single-step fluorocarbon plasma treatment-induced wrinkle structure for high-performance triboelectric nanogenerator, Small 12 (2016) 229–236.
[13] S. Yao, Y. Zhu, Wearable multifunctional sensors using printed stretchable conductors made of silver nanowires, Nanoscale 6 (2014) 2345–2352.
[14] J. Zhou, Y. Gu, P. Fei, W. Mai, Y. Gao, R. Yang, G. Bao, Z.L. Wang, Flexible piezotronic strain sensor, Nano Lett. 8 (2008) 3035–3040.
[15] J.M. Wu, C.-Y. Chen, Y. Zhang, K.-H. Chen, Y. Yang, Y. Hu, J.-H. He, Z.L. Wang, Ultrahigh sensitive piezotronic strain sensors based on a $ZnSnO_3$ nanowire/microwire, ACS Nano 6 (2012) 4369–4374.
[16] X. Cheng, B. Meng, X. Chen, M. Han, H. Chen, Z. Su, M. Shi, H. Zhang, Single-step fluorocarbon plasma treatment-induced wrinkle structure for high-performance triboelectric nanogenerator, Small 12 (2016) 229–236.
[17] X.-S. Zhang, M.-D. Han, R.-X. Wang, F.-Y. Zhu, Z.-H. Li, W. Wang, H.-X. Zhang, Frequency-multiplication high-output triboelectric nanogenerator for sustainably powering biomedical microsystems, Nano Lett. 13 (2013) 1168–1172.
[18] J. Luo, F.R. Fan, T. Zhou, W. Tang, F. Xue, Z.L. Wang, Ultrasensitive self-powered pressure sensing system, Extrem. Mech. Lett. 2 (2015) 28–36.
[19] J. Yang, J. Chen, Y. Liu, W. Yang, Y. Su, Z.L. Wang, Triboelectrification-based organic film nanogenerator for acoustic energy harvesting and self-powered active acoustic sensing, Acs Nano 8 (2014) 2649–2657.
[20] X. Chen, Y. Song, Z. Su, H. Chen, X. Cheng, J. Zhang, M. Han, H. Zhang, Flexible fiber-based hybrid nanogenerator for biomechanical energy harvesting and physiological monitoring, Nano Energy (2017).
[21] F.-R. Fan, L. Lin, G. Zhu, W. Wu, R. Zhang, Z.L. Wang, Transparent triboelectric nanogenerators and self-powered pressure sensors based on micropatterned plastic films, Nano Lett. 12 (2012) 3109–3114.
[22] H. Guo, J. Chen, L. Tian, Q. Leng, Y. Xi, C. Hu, Airflow-induced triboelectric nanogenerator as a self-powered sensor for detecting humidity and airflow rate, ACS Appl. Mater. Interfaces 6 (2014) 17184–17189.
[23] H. Baytekin, A. Patashinski, M. Branicki, B. Baytekin, S. Soh, B.A. Grzybowski, The mosaic of surface charge in contact electrification, Science 333 (2011) 308–312.
[24] Z. Su, M. Han, X. Cheng, H. Chen, X. Chen, H. Zhang, Asymmetrical triboelectric nanogenerator with controllable direct electrostatic discharge, Adv. Funct. Mater. 26 (2016) 5524–5533.
[25] J. Wang, C. Wu, Y. Dai, Z. Zhao, A. Wang, T. Zhang, Z.L. Wang, Achieving ultrahigh triboelectric charge density for efficient energy harvesting, Nat. Commun. 8 (2017).
[26] S. Niu, Y.S. Zhou, S. Wang, Y. Liu, L. Lin, Y. Bando, Z.L. Wang, Simulation method for optimizing the performance of an integrated triboelectric nanogenerator energy harvesting system, Nano Energy 8 (2014) 150–156.
[27] Y.S. Zhou, G. Zhu, S. Niu, Y. Liu, P. Bai, Q. Jing, Z.L. Wang, Nanometer resolution self-powered static and dynamic motion sensor based on micro-grated triboelectrification, Adv. Mater. 26 (2014) 1719–1724.
[28] Y. Li, G. Cheng, Z.-H. Lin, J. Yang, L. Lin, Z.L. Wang, Single-electrode-based rotationary triboelectric nanogenerator and its applications as self-powered contact area and eccentric angle sensors, Nano Energy 11 (2015) 323–332.
[29] H. Chen, L. Miao, Z. Su, Y. Song, M. Han, X. Chen, X. Cheng, D. Chen, H. Zhang, Fingertip-inspired electronic skin based on triboelectric sliding sensing and porous piezoresistive pressure detection, Nano Energy 40 (2017) 65–72.
[30] F.-R. Fan, Z.-Q. Tian, Z.L. Wang, Flexible triboelectric generator, Nano Energy 1 (2012) 328–334.
[31] J. Rychlewski, On Hooke's law, J. Appl. Math. Mech. 48 (1984) 303–314.
[32] J.T. Muth, D.M. Vogt, R.L. Truby, Y. Mengüç, D.B. Kolesky, R.J. Wood, J.A. Lewis, Adv. Mater. 26 (2014) 6307–6312.
[33] S. Gong, D.T. Lai, Y. Wang, L.W. Yap, K.J. Si, Q. Shi, N.N. Jason, T. Sridhar, H. Uddin, W. Cheng, Tattoolike polyaniline microparticle-doped gold nanowire patches as highly durable wearable sensors, ACS Appl. Mater. Interfaces 7 (2015) 19700–19708.
[34] J. Zhou, Y. Gu, P. Fei, W. Mai, Y. Gao, R. Yang, G. Bao, Z.L. Wang, Flexible piezotronic strain sensor, Nano Lett. 8 (2008) 3035–3040.
[35] M. Zu, Q. Li, Y. Zhu, Y. Zhu, G. Wang, J.-H. Byun, T.-W. Chou, Stress relaxation in carbon nanotube-based fibers for load-bearing applications, Carbon 52 (2013) 347–355.

Zongming Su received the B.S. degree from the University of Science and Technology Beijing (USTB) in 2013. He is currently pursuing the Ph.D. degree at the National Key Laboratory of Nano/Micro Fabrication Technology, Peking University, Beijing, China. His research interests are wearable electronics, stretchable sensors and micro/nano fabrication.

Hanxiang Wu is an undergraduate student in Microelectronics at Peking University, China. He majors in microelectronics and his research interests are self-powered sensors and energy harvesting technology.

Haotian Chen received the B. S. degree from Dalian University of Technology, China, in 2013. He is currently pursuing the Ph.D. degree at the National Key Laboratory of Nano/Micro Fabrication Technology, Peking University, Beijing, China. His research mainly focuses on energy harvesters and electronic skins.

Hang Guo received his B.S. degree from Huazhong University of Science and Technology (HUST) in 2017 and now is a Ph.D. student at Academy for Advanced Interdisciplinary Studies in Peking University. His research interests focus on electronic skin and self-powered nanosystems.

Xiaoliang Cheng received the B.S. degree from the University of Electronic Science and Technology of China, Chengdu, in 2014. He is currently pursuing the Ph.D. degree at the National Key Laboratory of Nano/Micro Fabrication Technology, Peking University, Beijing, China. His research interests mainly include design and fabrication of nanogenerator and mechanical energy harvester.

Yu Song received the B.S. degree in Electronic Science & Technology from Huazhong University of Science and Tech-nology, China, in 2015. He is currently pursuing the Ph.D. de-gree at the National Key Laboratory of Nano/Micro Fabrica-tion Technology, Peking University, Beijing, China. He majors in MEMS and his research is focusing on supercapacitors and self-charging power system.

Xuexian Chen received the B.S. degree from the University of Electronic Science and Technology of China, Chengdu, in 2015. She is currently pursuing the Ph.D. degree at the National Key Laboratory of Nano/Micro Fabrication Technology, Peking University, Beijing, China. Her research interests mainly include design and fabrication of hybrid nanogenerator and electrospinning process.

Haixia (Alice) Zhang received the Ph.D. degree in mechanical engineering from Huazhong University of Science and Technology, Wuhan, China, 1998. She is currently a Professor with the Institute of Microelectronics, Peking University, Beijing, China. She joined the faculty of the Institute of Microelectronics in 2001 after finishing her post-doctoral research in Tsinghua University. Her research interests include MEMS design and fabrication technology, SiC MEMS, and micro energy technology.